Editors' Suggestion

High-field/high-frequency electron spin resonances of Fe-doped β-Ga₂O₃ by terahertz generalized ellipsometry: Monoclinic symmetry effects

Steffen Richter, 1,2,* Sean Knight, 1,2 Oscar Bulancea-Lindvall, 3 Sai Mu, 4,5 Philipp Kühne, 6 Megan Stokey, 7 Alexander Ruder , Viktor Rindert , Viktor Ivády , 3,8,9 Igor A. Abrikosov , Chris G. Van de Walle , 4 Mathias Schubert, 1,7 and Vanya Darakchieva 1,2,†

¹Competence Center for III-Nitride Technology, C3NiT-Janzén, Solid State Physics and NanoLund, Lund University, Box 118, 22100 Lund, Sweden

²Competence Center for III-Nitride Technology, C3NiT-Janzén, Department of Physics, Chemistry and Biology (IFM), Linköping University, 58183 Linköping, Sweden

> ³Department of Physics, Chemistry and Biology (IFM), Linköping University, 58183 Linköping, Sweden ⁴Materials Department, University of California, Santa Barbara, California 93106-5050, USA ⁵Department of Physics and Astronomy, University of South Carolina, Columbia 29208, USA

⁶Competence Center for III-Nitride Technology, C3NiT-Janzén, Department of Physics, Chemistry and Biology (IFM), Linköping University, 58183 Linköping, Sweden

⁷Department of Electrical and Computer Engineering, University of Nebraska-Lincoln, Lincoln, Nebraska 68588, USA ⁸Department of Physics of Complex Systems, Eötvös Loránd University, Egyetem tér 1-3, H-1053 Budapest, Hungary 9 MTA–ELTE Lendület "Momentum" NewQubit Research Group, Pázmány Péter, Sétány 1/A, 1117 Budapest, Hungary



(Received 10 November 2023; revised 30 April 2024; accepted 6 May 2024; published 13 June 2024)

We demonstrate detection and measurement of electron paramagnetic spin resonances (EPR) of iron defects in β -Ga₂O₃ utilizing generalized ellipsometry at frequencies between 110 and 170 GHz. The experiments are performed on an Fe-doped single crystal in a free-beam configuration in reflection at 45° and magnetic fields between 3 and 7 T. In contrast with low-field, low-frequency EPR measurements, we observe all five transitions of the s = 5/2 high-spin state Fe³⁺ simultaneously. We confirm that ferric Fe³⁺ is predominantly found at octahedrally coordinated Ga sites. We obtain the full set of fourth-order monoclinic zero-field splitting parameters for both octahedrally and tetrahedrally coordinated sites by employing measurements at multiple sample azimuth rotations. The capability of high-field EPR allows us to demonstrate that simplified secondorder orthorhombic spin Hamiltonians are insufficient, and fourth-order terms as well as consideration of the monoclinic symmetry are needed. These findings are supported by computational approaches based on density-functional theory for second-order and on ligand-field theory for fourth-order parameters of the spin Hamiltonian. Terahertz ellipsometry is a way to measure spin resonances in a cavity-free setup. Its possibility of varying the probe frequency arbitrarily without otherwise changing the experimental setup offers unique means of truly disentangling different components of highly anisotropic spin Hamiltonians.

DOI: 10.1103/PhysRevB.109.214106

I. INTRODUCTION

The monoclinic wide-band gap semiconductor β -Ga₂O₃ is a very promising material for high power electronics that has been studied intensively in recent years [1–8]. Breakdown voltages as high as 8 MV/cm are possible due to the large band gap of about 5 eV, which makes it superior to other

Published by the American Physical Society under the terms of the Creative Commons Attribution 4.0 International license. Further distribution of this work must maintain attribution to the author(s) and the published article's title, journal citation, and DOI. Funded by Bibsam.

wide-gap semiconductors such as GaN and SiC. As-grown, unintentionally doped material is n type with typical chargecarrier concentrations on the order 10¹⁷ cm⁻³ due to, e.g., oxygen vacancies, unintentional incorporation of Si, and other defect-related mechanisms [9–11]. Doping with Fe is most common to obtain semi-insulating material [7,12-14]. Iron creates a deep compensating acceptor that pins the Fermi level at about 0.8 eV below the conduction band [12,15,16]. For monoclinic β -Ga₂O₃ (space group no. 12, $C_{2h}^3 \equiv C2/m$), the question arises how its low structural symmetry affects its physical properties. Serving as a prototype monoclinic semiconductor whose underlying material physics is thoroughly explored presently, many new properties have already been discovered. For example, infrared dipole moments of lattice vibrations do not coincide with high-indexed crystallographic axes [17,18]. Free charge carriers do not only screen longitudinal optical phonons but also change their dipole directions continuously with frequency and depending on the

^{*}steffen.richter@ftf.lth.se; Present address: SCHOTT AG, Advanced Optics, Hattenbergstr. 10, 55122 Mainz, Germany.

[†]vanya.darakchieva@ftf.lth.se

free-charge-carrier concentration [19]. Optical properties have also been studied in the THz range [20,21] and THz ellipsometry was used to obtain the quasistatic permittivity and its principal directions [22]. Studies in the visible to deep ultraviolet spectral range have revealed band gap order, excitonic effects, and peculiarities of singular optic axes [23–25].

Due to its important role for the material's electrical insulating properties, Fe_{Ga} with local monoclinic $C_s \equiv m$ symmetry is a suitable electronic defect to investigate the relations between reduced symmetry and macroscopic electronic properties. Extrinsic electronic defects in β -Ga₂O₃ have been widely investigated by electron paramagnetic spin resonance (EPR) spectroscopy [26-37]. Similarly to Ir and Cr, Fe is often unintentionally incorporated in β -Ga₂O₃ and shows strong EPR signals [38]. Fe can reside on tetrahedrally coordinated Gai or octahedrally coordinated Gaii sites where the latter is commonly reported as the preferred one [39,40]. Transition metals are often high-spin systems. So is the neutral ferric Fe^{3+} with five unpaired 3d electrons. The total electron spin s = 5/2 results in a sextet of projections $m_s = -5/2, \dots, +5/2$ which gives rise to five transitions with $\Delta m_s = \pm 1$. EPR of Fe³⁺ in β -Ga₂O₃ is characterized by large zero-field, or fine-structure, splittings (ZFS) of several tens of GHz [36,39,41], similar to Cr [42,43]. Therefore, no reported EPR survey of Fe in β -Ga₂O₃ in X or Q bands could capture all five transitions in one B-field scan without rotating the sample relative to the magnetic-field orientation. Ferric Fe³⁺ is the neutral, nonactived dopant state and turns into ferrous Fe²⁺ when capturing electrons and hence acting as a compensating acceptor [16]. This charge transition has been studied by photo-EPR experiments that monitor the effect of illumination [14,32,33,36,37]. The ratio of Fe^{2+} to Fe^{3+} is related to the activation of donors such as oxygen vacancies and Ir ions. In fact, Fe is amphoteric and can also establish a deep donor as Fe⁴⁺ [44] (see also Fig. 4).

In this paper, we use frequency-varying quasi-optical (sub) THz electron-paramagnetic-resonance generalized ellipsometry to investigate Fe defects in β -Ga₂O₃.

II. MONOCLINIC s = 5/2 SPIN HAMILTONIAN

In monoclinic β -phase gallium oxide, Ga^{3+} ions occupy distorted tetrahedral (Ga_{ii}) and octahedral (Ga_{ii}) sites. Substitutional Fe³⁺ ions have two 4s valence electrons and one 3d electron involved in bondings with neighboring oxygen atoms. The iron ions then have five unpaired 3d electrons (half filled 3d shell) left with total spin s = 5/2. The full spin Hamiltonian for s = 5/2 with monoclinic local site symmetry with the high-symmetry direction (here b) parallel to z reads [41,45]:

$$\hat{H} = \mu_{\rm B} \vec{B} \hat{g} \vec{s} + B_2^0 O_2^0 + B_2^2 O_2^2 + B_2^{-2} O_2^{-2}$$

$$+ B_4^0 O_4^0 + B_4^2 O_4^2 + B_4^{-2} O_4^{-2}$$

$$+ B_4^4 O_4^4 + B_4^{-4} O_4^{-4},$$
(1)

where the first term represents the Zeeman splitting with Bohr magneton $\mu_{\rm B}$ and g-factor tensor \hat{g} , and O_k^q are Stevens (equivalent) operators. The (real-valued) Stevens coefficients B_k^q represent different symmetry distortions due to ZFS [46]. See the Supplemental Material [47] for further details on

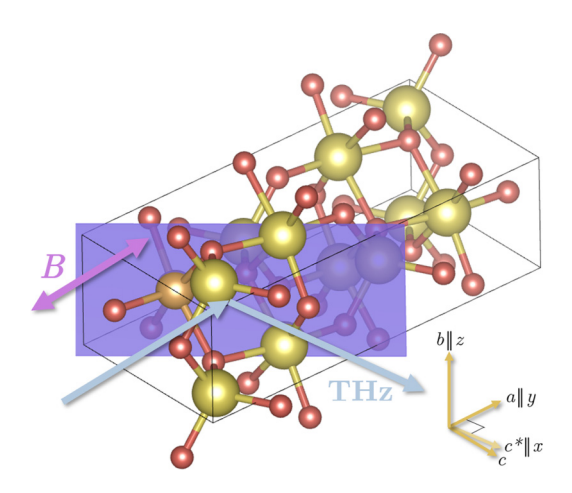


FIG. 1. Sketch of the monoclinic C2/m unit cell (monoclinic angle of about 104° between a and c) and the experimental configuration. Large greenish atoms represent Ga, small reddish atoms oxygen. One Ga_{ii} atom with octahedral coordination is replaced here by an Fe atom (golden). The sample surface is parallel to $(\bar{2}01)$, the THz beam is reflected at an angle of incidence of 45° , the external B field is oriented parallel to the incident light. For different scans, the sample was rotated about its $(\bar{2}01)$ surface normal. Drawing produced with the help of VESTA [48]. The tripod indicates only principal directions, arrow lengths are arbitrary.

the Stevens formalism and how O_k^q relate to the underlying coordinate system (x, y, z). Rotation of the coordinate system around the high-symmetry axis z redistributes the coefficients with nonzero index q. At least one coefficient (commonly B_2^{-2}) can be nulled through appropriate choice of the coordinate system (standardization [45,49]) but generally all entries are nonzero. Also the \hat{g} factor is anisotropic, with the principal directions (x', y', z) independent of ZFS coordinate system except for the high-symmetry direction z. Here, we chose the coordinate system such that it holds for β -Ga₂O₃: $x||c^*$, y||a, and b||z, where c^* is the reciprocal-lattice vector to c such that c^* is perpendicular to a (see Fig. 1).

In the literature, the following simplified electron-spin Hamiltonian is often found [36,37,39]:

$$\hat{H} = \mu_{\rm B} \vec{B} \hat{g} \vec{s} + \vec{s} \hat{D} \vec{s}
= \mu_{\rm B} \vec{B} \hat{g} \vec{s} + D \left(s_z^2 - \frac{1}{3} s(s+1) \right) + E \left(s_x^2 - s_y^2 \right)
= \mu_{\rm B} \vec{B} \hat{g} \vec{s} + B_2^0 \left[3 s_z^2 - s(s+1) \right] + B_2^2 \left(s_x^2 - s_y^2 \right)
= \mu_{\rm B} \vec{B} \hat{g} \vec{s} + B_2^0 O_2^0 + B_2^2 O_2^2.$$
(2)

Here, the traceless ZFS tensor \hat{D} can be parametrized by parameters D and E representing (uni-)axial and transverse rhombic distortions due to spin-spin and spin-orbit interactions, respectively [50]. The spin projection operators $s_{x,y,z}$ illustrate the meaning of the equivalent operators O_k^q . In some reports, scaled Stevens coefficient b_k^q with $b_2^q = 3B_2^q$, $D = b_2^0 = 3B_2^0$, and $E = B_2^2$ are used. Equation (2) is an approximation in two ways: Restriction to second-order terms (k = 2) approximates the k = 5/2 system as k = 3/2 one. And neglecting negative index terms (k = 2) reduces the complexity to orthorhombic symmetry. This implies that the principal

directions of \hat{g} have to line up with the ZFS coordinate system in Eq. (2), (x', y')||(x, y).

III. EXPERIMENTAL DETAILS

We measure THz EPR generalized ellipsometry in a freebeam reflection geometry at an angle of incidence of 45°, using an in-house built ellipsometer [51]. The static magnetic field is applied parallel to the incident light, as depicted in Fig. 1. The detection of EPR transitions by ellipsometry is based on the underlying circular dichroism and related birefringence. It arises from a transition with $\Delta m_s = \pm 1$ requiring transfer of angular momentum and hence absorption of only right or left circularly polarized light [52]. In the case of EPR, no electric- but a magnetic-dipole transition occurs. Accordingly, circularly polarized resonances do not appear in the dielectric function tensor $\hat{\varepsilon}(f)$ but in the magnetic permeability tensor $\hat{\mu}(f, \vec{B})$. While both tensors are frequency-dependent (f), $\hat{\mu}$ will also depend on the static external magnetic field \vec{B} . For $\vec{B} \parallel \vec{e}_z$ and assuming $\hat{\mu}$ being identity matrix if no EPR resonance occurs, it holds [52]

$$\hat{\mu} = \begin{pmatrix} \frac{1}{2}(1 + \mu_{\text{EPR}}) & \mp \frac{i}{2}(1 - \mu_{\text{EPR}}) & 0\\ \pm \frac{i}{2}(1 - \mu_{\text{EPR}}) & \frac{1}{2}(1 + \mu_{\text{EPR}}) & 0\\ 0 & 0 & 1 \end{pmatrix}, \quad (3)$$

which is generally valid for any \vec{B} direction with respective rotation of the coordinate system. Equation (3) reflects that the permeability for one circular polarization remains at a constant value of one (unaltered) while spin transitions appear only in the other circular polarization which is associated with a magnetic permeability $\mu_{\rm EPR}(f,\vec{B})$. EPR transitions can be described by Lorentzian resonances [52]:

$$\mu_{\text{EPR}}(f, \vec{B}) = 1 + \sum_{k} \frac{A_{0,k}}{f_{r,k}(\vec{B})^2 - f^2 - if\gamma_{0,k}},$$
 (4)

with resonance frequencies $f_{r,k}(\vec{B})$ defined by the spin splitting under the specific direction of \vec{B} with respect to the crystal [cf. Eq. (1)], broadening parameters $\gamma_{0,k}$ and $A_{0,k}$ being amplitude factors. Equation (4) defines resonances in f-domain EPR. It can equally be expressed for B-domain EPR as

$$\mu_{\text{EPR}}(f, \vec{B}) = 1 + \sum_{k} \frac{A_k}{-B_{r,k}(f, \vec{e}_B)^2 + B^2 - i|B|\gamma_k}, \quad (5)$$

where $B_{r,k}$ is the resonance field and \vec{e}_B is the direction of \vec{B} , and amplitude A_k and broadening γ_k are redefined with respect to $A_{0,k}$ and $\gamma_{0,k}$. Generally, all amplitude and broadening constants will differ for different transitions, depending also on f and \vec{B} . Note that, as a result of having either the frequency f or the magnetic field strength B as free variable, the signs

in the denominator are seemingly different in Eqs. (4) and (5). This implies generally that, at a given nonzero field \vec{B} , $\text{Re}(\mu_{\text{EPR}}(f=0)) > \text{Re}(\mu_{\text{EPR}}(f=\infty))$, but at a given frequency f, $\text{Re}(\mu_{\text{EPR}}(B=0)) < \text{Re}(\mu_{\text{EPR}}(|B|=\infty))$.

The EPR resonances in $\hat{\mu}(f, \vec{B})$ are imprinted in the optical response to a plane-wave probe $\vec{\mathcal{B}}_1 e^{-2\pi i f t}$ and can be measured in polarization-resolved frequency- or fieldscanning reflection and transmission experiments. In this paper, we present EPR ellipsometry measurements carried out by scanning the external magnetic field \vec{B} at different constant frequencies f, i.e., field-domain EPR. Scanning Bof Eq. (5) is equivalent to scanning f_r in Eq. (4). In contrast with conventional EPR spectroscopy we are not measuring a differential cross-polarized reflection or transmission signal. Instead, the Müller matrix is measured, which describes generally the change of incident light polarization upon reflection or transmission [51,53,54]. Our THz ellipsometer is capable of measuring the upper left 3×3 submatrix but not the last row and column of the 4×4 Müller matrix [51]. As can be seen from Eq. (4), the optical response is not only affected at resonance $(f = f_r)$ but particularly the real part of μ_{EPR} alters the refractive index $n = \sqrt{\varepsilon \mu_{\rm EPR}}$ for light of the resonant circular polarization. In a simplified manner, ε shall be a (isotropic) dielectric-function value here, that applies to circularly polarized light at the particular propagation direction. Hence, the optical response is altered also in the vicinity of a resonance in f- or B-domain measurements. This renders ellipsometry very sensitive to the EPR transitions through accurate measurements of refractive-index variation. Neither magnetic field modulation with lock-in detection is applied nor is a special microwave-cavity used here. Intrinsically, ellipsometry at oblique angle of incidence represents here a mixture of parallel- and perpendicular-mode EPR [50,55]. Although with incident light being parallel to \vec{B} , which would correspond to perpendicular mode, the 45° reflected light direction will always have a $\vec{\mathcal{B}}_1$ component parallel \vec{B} of the transverse-electric (TE) polarization.

The investigated samples are commercially available Fedoped bulk single crystals obtained by edge-defined film-fed growth [56,57] (Novel Crystal Technology, Inc.). Electrical resistivity is specified to be $\geqslant 1 \times 10^{10} \ \Omega$ cm. The investigated bulk substrates of about $10 \times 15 \ \text{cm}^2$ area and 0.5 mm thickness have ($\bar{2}01$) and (010) surface planes.

A total set of five different sample orientations of the $(\bar{2}01)$ sample (rotated about its surface normal), each at five different frequencies f = (110, 125, 149, 155, 170) GHz were measured in reflection while the sample was clamped onto a metal plate. For two orientations, the B field is applied exactly within the monoclinic ac plane. For other orientations, the angle between \vec{B} and the ac plane increases to at most 45°. Additionally, the (010)-oriented sample was measured at slightly different frequencies in transmission configuration at normal incidence, with \vec{B} parallel to the crystallographic b axis. All measurements were carried out at a nominal temperature of 17 K in a cryostat hosting an 8 T superconducting magnet with optical access (Cryogenics Ltd. London, UK). The magnetic field was calibrated and corrected by means of measuring EPR on 1,1-diphenyl-2-picryl-hydrazyl (DPPH) as standard reference sample. For the B field scans, we find the noise level for the Müller matrix elements M₂₃, M₃₂, M₂₂,

 $^{^{1}}$ We note that the Lorentzian oscillator is a matter of choice here, and also $\mu_{\text{EPR}}(f,\vec{B}) = 1 + \sum_{k} A'_{0,k}/[f_{r,k}(\vec{B}) - f - i\gamma'_{0,k}]$ is often applied in EPR contexts. Both parametrizations are equivalent if $f \approx f_{r,k}$. We note that $\gamma'_{0,k}$ refers to the half-width at half maximum of the resonance peak in μ_{EPR} , while $\gamma_{0,k}$ of the Lorentzian oscillator (4) refers to its full width.

and M_{33} , on order ± 0.001 for M_{13} , M_{31} , M_{12} , and M_{21} on order ± 0.01 . Additionally, drifts on order ± 0.01 may occur within several hours for all elements. Conventional optical modeling using a transfer-matrix formalism was hindered by distortions on the present Müller matrix data that arise from diffraction of sample edges, cryostat windows, and abovementioned drifts. While we expect the EPR features most pronounced in M_{23} and M_{32} scans [52], optical anisotropy and mentioned distortions can shift them to different Müller matrix elements. For simplicity, the lineshape of the Müller matrix scans $M_{ij}(B)$ were modeled empirically by series of phase-shifted Lorentzian resonances:

$$M_{ij}(B) = M_{ij}^0 + \text{Re}\left(e^{i\phi_{ij}} \sum_k \frac{A_{ij,k}}{-B_{r,k}^2 + B^2 - i|B|\gamma_B}\right),$$
 (6)

where the sum runs over all transitions of the two times five observed resonance lines of Fe³⁺. We note that depending on the considered Müller matrix element and frequency, the line-shapes can resemble either directly Lorentzian peaks or dips (phase $\phi \approx \pm \pi/2$) or derivative-like shapes ($\phi \approx 0, \pi$). The broadening γ_B is assumed constant for all transitions in one individual B scan here. Throughout this paper, all presented Müller matrix elements are normalized by M_{11} , which itself was not included in the evaluation.

A numerical optimizer was used to fit the g factor and second-order ZFS parameters as well as their principal directions in the monoclinic ac plane. For all frequencies and orientations, eight Müller matrix scans as well as TE and TM (transverse magnetic) copolarized reflectance scans were simultaneously included in the fitting process. Lineshapes of the reflectance data were treated equally as for the Müller matrix data. In each iteration of the optimization, the ten resonance fields $B_{r,k}$ and relative amplitudes $A_{ij,k}$ for each applied frequency were computed using EASYSPIN [58] based on a set of spin Hamiltonian parameters according to Eq. (1), sample temperature and sample orientation (including alignment off-angles). The lineshapes were constructed using these parameters along with auxiliary parameters ϕ_{ij} , γ_B , and an amplitude scaling parameter for each data type in every dataset. The baselines of each scan should be constant values but were also modeled by a B-dependent spline function to correct for underlying drifts that occurred during the scans. All parameters were optimized in order to minimize the sum of squared error (SSE) defined by the difference between modeled and measured lineshape. A flow chart illustrating the algorithm is shown in the Supplemental Material [47].

IV. THEORETICAL CALCULATIONS

The computation of ZFS in anisotropic crystals from first principles is very challenging. The origin of the ZFS is not only spin-spin but also spin-orbit interaction [59,60]. We have also applied density function theory (DFT) calculations to find a first-principles second-order approximation to the ZFS of Fe^{3+} on Ga_{ii} sites. And we have applied crystal-ligand field theory (CLFT) as implemented in the *PyCrystalField* toolbox [61] following the method of Hutchings [62] to obtain a qualitative fourth-order approximation for the ZFS parameters of Fe^{3+} on both Ga sites.

We also performed DFT calculations to investigate the actual incorporation of Fe impurities in β -Ga₂O₃ and its physical properties. The calculations were performed using the projector augmented wave method (PAW) [63] implemented in the Vienna ab initio simulation package (VASP) [64,65]. A plane-wave energy cutoff of 400 eV was employed and Brillouin-zone (BZ) integration was carried out using a Γ -centered $4 \times 4 \times 4$ k-point mesh for the primitive cell. The fully filled 3d states on Ga are treated as core states. To correctly describe the electronic structure and charge localization, we use the hybrid functional of Heyd, Scuseria, and Ernzerhof (HSE) [66,67], with a mixing parameter of $\alpha = 0.32$. This produces a band gap of 4.83 eV for β -Ga₂O₃. A $1 \times 3 \times 2$ supercell of 120 atoms was built based on the conventional cell (see Fig. 1) for the defect calculations, and a single k point at (0.25, 0.25, 0.25) was used for the BZ integration in the supercell. The formation energy of Fe is calculated as

$$E^{f}(\operatorname{Fe}_{\operatorname{Ga}}^{q}) = E_{\operatorname{tot}}(\operatorname{Fe}_{\operatorname{Ga}}^{q}) - E_{\operatorname{tot}}(\operatorname{Ga}_{2}\operatorname{O}_{3})$$
$$- (\mu_{\operatorname{Fe}} + \mu_{\operatorname{Fe}}^{0}) + (\mu_{\operatorname{Ga}} + \mu_{\operatorname{Ga}}^{0})$$
$$+ q(E_{\operatorname{F}} + E_{VBM}) + \Delta^{q}, \tag{7}$$

where $E_{\rm tot}({\rm Fe}_{\rm Ga}^q)$ is the total energy of one ${\rm Fe}_{\rm Ga}$ in charge state q in the supercell, $E_{\rm tot}({\rm Ga}_2{\rm O}_3)$ is the total energy of the bulk supercell, and $E_{\rm F}$ is the Fermi energy, referenced to the valence-band maximum (E_{VBM}) . Δ^q is a finite-size correction term for charged defects [68,69]. $\mu_{\rm Fe}^0$ and $\mu_{\rm Ga}^0$ are total energies of the elemental phase Fe and Ga. The Ga and O chemical potentials have to fulfill the stability condition for bulk ${\rm Ga}_2{\rm O}_3$: $2\mu_{\rm Ga}+3\mu_{\rm O}=H_f({\rm Ga}_2{\rm O}_3)$, where $H_f({\rm Ga}_2{\rm O}_3)=-10.22$ eV is the formation enthalpy of ${\rm Ga}_2{\rm O}_3$. Under Ga-rich condition, the limit for $\mu_{\rm Fe}$ is chosen to be Fe metal.

A. Second-order zero-field splitting from first principles

DFT was applied to compute the second-order ZFS as in Eq. (2) for Fe^{3+} on Ga_{ii} sites. The spin-spin dipolar contribution to the ZFS was calculated as described in Refs. [60,70–73], while the spin-orbit interaction (SOI) induced ZFS was calculated from mapping the total energies (with SOI) of different spin orientations to the spin Hamiltonian [71–73]. See the Supplemental Material [47] for details. The SOI-induced ZFS is equivalent to calculating the single ion anisotropy for the spin state of the defect. The spin Hamiltonian associated with the single-ion anisotropy is defined as

$$\hat{H}_{D} = \vec{s}\hat{D}\vec{s}$$

$$= -D_{xx}s_{x}^{2} - D_{yy}s_{y}^{2} - D_{zz}s_{z}^{2}$$

$$-D_{xy}(s_{x}s_{y} + s_{y}s_{x}) - D_{xz}(s_{x}s_{z} + s_{z}s_{x})$$

$$-D_{yz}(s_{y}s_{z} + s_{z}s_{y}). \tag{8}$$

The parameters $D_{\alpha\beta}$ can be computed by the four-state mapping method [72,73]:

$$D_{\alpha\beta} = -\frac{1}{4s^2} \left(E_{\alpha\beta}^{(1)} - E_{\alpha\beta}^{(2)} - E_{\alpha\beta}^{(3)} + E_{\alpha\beta}^{(4)} \right), \tag{9}$$

where $E_{\alpha\beta}$ are fully relativistic total energies for different spin orientations (see the Supplemental Material of Ref. [73] for more details).

It turns out that more than 90% of the contributions arises from spin-orbit interaction. With the half filled 3d shell, the total orbital momentum of the electrons will be zero if the crystal fields are not large. This is referred to as *S-state ion* behavior and would result in suppression of interaction between the crystal field and orbital momenta. However, particularly for iron, screening of the 3d orbitals is very little and the crystal-field interaction is therefore greatly enhanced [55].

B. Qualitative estimates of fourth-order zero-field splitting

CLFT was used to calculate fourth-order Stevens coefficients for the monoclinic Fe_{Ga} system. This approach allows for qualitative insights into local site distortion of the Hamiltonian by foreign ions in a relaxed unit cell. As only a point-charge-like electrostatic perturbation of the electron Hamiltonian by the ions of the host-crystal is taken into account, it is not expected that the results match quantitatively. Yet, they will give a first-order approximation for the ratios of ZFS parameters of the same order [62]. The ligand fields from nearby oxygen and gallium atoms are expected to particularly imprint the symmetry onto the Stevens coefficients. However, the effect of screening is neither included in this model nor known. Hence, we included only the field contribution of nearest-neighbor sites in this analysis.

DFT calculations were performed in order to relax a 1440-atom defect structure ($2 \times 8 \times 4$ conventional cell) at the Γ point using the PBE-sol functional [74]. Simulations were carried out with an energy cutoff of 700 eV until forces were less than 1×10^{-2} eV/Å. The obtained Ga_i defect structure featured Fe-O bond lengths of size 1.87 Å for three out of the four nearest neighbors. The fourth bond, lying in the ac plane, was elongated at 1.92 Å. For the Ga_{ii} site, we obtain bond lengths of 1.88 and 1.94 Å along the a axis, and 1.92 and 1.99 Å in the remaining directions, which are constrained by the mirror symmetry in the ac plane.

V. RESULTS AND DISCUSSION

The high frequencies and a wide range of magnetic field allow us to observe all ten transition of the s = 5/2 system Fe³⁺ (five transitions associated with the tetrahedral Ga_i sites, five with the octahedral Gaii sites) simultaneously in the ellipsometry data of each B field scan. Figures 2 and 3 are representative examples of Müller matrix EPR field scans at varying frequency and sample orientation, respectively. The EPR signatures are imprinted in nearly all Müller matrix types but notably strongest in M_{23} and M_{32} , which represent linear retardation arising from the EPR-induced circular dichroism [54]. Example figures with complete sets of all measured Müller matrix elements are shown in the Supplemental Material [47]. For each scan shown in Fig. 2, we can identify two sets of five lines each, as highlighted by the symbols close to the line that represents the measurement at 125 GHz. The stronger set arises from Fe³⁺ on octahedrally coordinated Gaii sites and the weaker one from Fe³⁺ on tetrahedrally coordinated Ga_i sites [39]. The ZFS is directly visible in Fig. 2 through the splitting of the transitions (different g_{eff}) and frequency-dependent values of g_{eff} . All g_{eff} values approach the actual g-factor value for the given \vec{B} direction when f

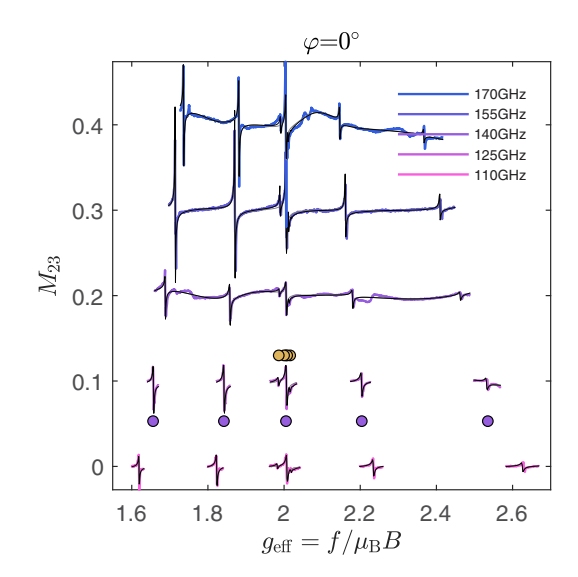


FIG. 2. Example EPR ellipsometry scans at five different frequencies f measured at fixed sample orientation $\varphi = 0^{\circ}$ as depicted in Fig. 1. Data are plotted against effective g factor geff to allow stacking scans from different B ranges. Shown is the background-subtracted Müller matrix element M_{23} . Data from different orientations are offset by 0.1 each. Two sets of five resonances each are visible as illustrated by markers for the 125 GHz dataset as example. The resonances originate from Fe³⁺ on octahedrally coordinated (stronger widely separated resonances, violet markers) and tetrahedrally coordinated (weaker resonances around $g_{\text{eff}} = 2$, yellow markers) Ga sites. Black (gray) lines show modeling including both (only the strong) transitions. Visible artifacts and baseline drifts arose from system instabilities during the measurements. Similar data were obtained at multiple sample azimuthal angles (cf. Fig. 3). A similar plot with the x scale zoomed to the range around two can be found in the Supplemental Material [47].

increases and the Zeeman term becomes more dominant. This emphasizes the capability of distinguishing anisotropic \hat{g} and ZFS effects through measurements at varying the frequency. Example splittings of the spin states with varying frequency and crystal orientation are illustrated in the supplement. Transitions at a given frequency are indicated therein and can be directly mapped to Figs. 2 and 3.

Although we did not apply any modulation scheme, the resonance shapes look derivative-like in most Müller matrix elements. The features in the measured data can also turn into peak- or dip-like shapes for other Müller matrix elements (see the Supplemental Material [47]). The relative intensity of the spin transition within a quintuplet of transitions is directly related to the Boltzmann distribution at the sample temperature of 17 K and the sign of B_2^0 . These relative intensities are predicted by the model and are directly matching the measured data without further adjustments.

The relative intensity of transitions associated with Ga_i and Ga_{ii} sites represents the respective distribution of the Fe ions. From modeling, we obtain a ratio for Ga_i/Ga_{ii} site occupation of approximately 15%. Meil'man reported for X-band EPR on a Verneuil-method-grown single crystal with 0.1 at.% Fe incorporation a ratio of 1/2 [41]. Büscher and Lehmann reported approximately 20% using X-band and Q-band EPR for crystals grown from the flux [39]. Formation

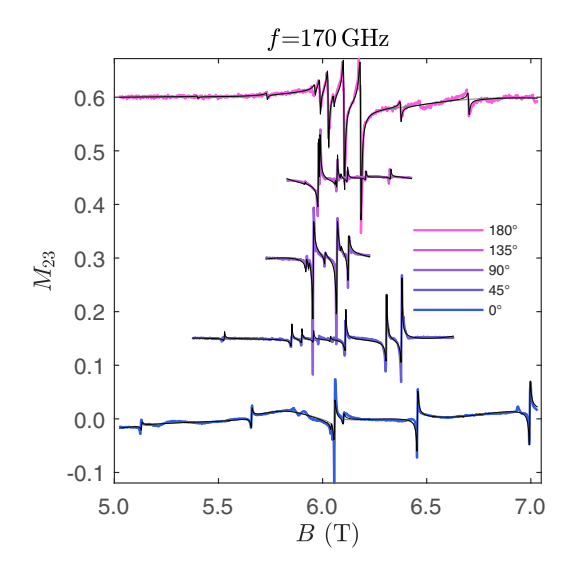


FIG. 3. Example EPR ellipsometry scans carried out at f=170 GHz at different sample rotations φ around its surface normal according to the legend. Orientation 0° corresponds to the situation in Fig. 1. The Müller matrix element M_{23} is shown after background subtraction and different lines are offset by 0.15 each. The blue line labeled for 0° sample azimuth represents the same data as shown in Fig. 2 for 170 GHz. The two sets of five resonances belonging to Fe³⁺ on octahedral Ga_i (strong amplitudes) and tetrahedral Ga_{ii} (weaker amplitudes) sites are seen. Black (gray) lines show modeling including both (only the strong) transitions. Similar data were obtained for each orientation at multiple frequencies (cf. Fig. 2).

energy calculations of Fe_{Ga} are consistent with the experimental observations: they show that incorporation of Fe on octahedral Ga_{ii} sites is energetically preferable to tetrahedral Ga_{i} sites by approximately 0.1 eV. Figure 4 depicts the DFT results, showing these small differences for the different sites.

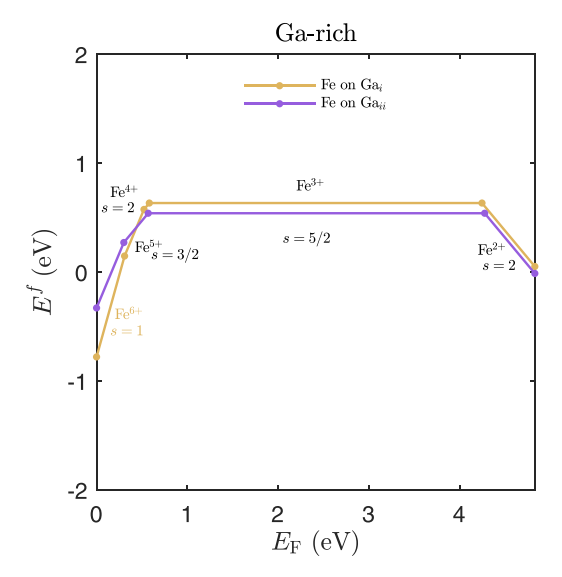


FIG. 4. Formation energy E^f of Fe_{Ga} versus Fermi level E_F for β -Ga₂O₃ under Ga-rich conditions. Fe incorporation on both Ga_i and Ga_{ii} sites is considered. The spin and charge state has been labeled.

Already previous DFT calculations [13] demonstrated this.² Yet, Fe incorporation on the tetrahedral Ga_i and octahedral Ga_{ii} sites exhibit both comparably low formation energy. Figure 4 shows also that the Fe impurity turns into the single acceptor Fe²⁺ with spin state s = 2 in the n-type doping limit. The related (0/-) charge-state transition levels occur at 0.56 and 0.59 eV below the conduction band minimum. For the neutral Fe³⁺ with a half filled 3d shell, the high spin state s = 5/2 is obtained for both Fe on Ga_i and Ga_{ii} sites.

Comparing the resonance amplitudes for measurements at different frequencies in Fig. 2 reveals a maximum around 155 to 160 GHz, where amplitudes reach up to 0.2 in the Müller matrix at most. For 110 GHz, amplitudes drop to about 0.04 only. We expect that the single-crystal substrates act as a cavity themselves, as observed before [52]. Then, approximately one Fabry-Pérot oscillation appears in the frequency range 110–170 GHz. The cavity effect enhances the amplitudes accordingly, but the resonances can even be measured when not in resonance with the standing waves inside the crystal.

Modeling is carried out involving all measured data simultaneously and modeled lineshapes are also shown in Figs. 2 and 3 as black and gray lines. The match of modeled and experimental data is close but not perfect. However, it should be emphasized that all resonance fields and amplitudes for all measured sample orientations, frequencies and data types (Müller matrix elements) are simultaneously modeled because they are all at once determined by the spin Hamiltonian. Only the exact sample orientation (small but very relevant off-angles for sample azimuth and tilt), the absolute amplitude scaling, and a line broadening are further fit parameters. In fact, the observed broadening values of approximately 4–5 mT are mostly caused by the B inhomogeneity of the magnet which is specified to be up to 3000 ppm within a 1 cm cylindrical volume at the sample position. In conventional EPR system, changing the sample azimuth angle results in the B-field orientation being rotated within a plane with respect to the crystal. In our experimental configuration, the B field and sample normal are at an angle of 45°. Consequently, the B orientation is moving on a cone relative to the crystal. This allows us to obtain sufficient linearly independent measurement data to over-constrain the mathematical problem of disentangling anisotropic effects within the monoclinic plane and effects parallel to the high-symmetry direction b. While configurations with the B field applied parallel to the monoclinic plane are affected by all B_k^q coefficients, only those with q = 0 imprint in the B||b configurations. Figure 5 illustrates the complexity of the resonance evolution upon sample azimuth rotation. Symbols and symbol sizes here indicate resonance field values and amplitudes, respectively, as obtained from an individual lineshape analysis of the measurements. Lines and their thickness indicate also resonance fields and amplitudes, and are based on the Hamiltonian parameters found from global modeling with respect to Eq. (1). We

²The charge state transitions levels shown in Fig. 4 and reported in to Ref. [13] are similar, the generally higher (by approximately 1 eV) formation energies for both Ga sites have been cross-checked and are due to the choice of the limiting phase. While Ga₃Fe was used as the limiting phase under Ga-rich conditions in Ref. [13], we use Fe here.

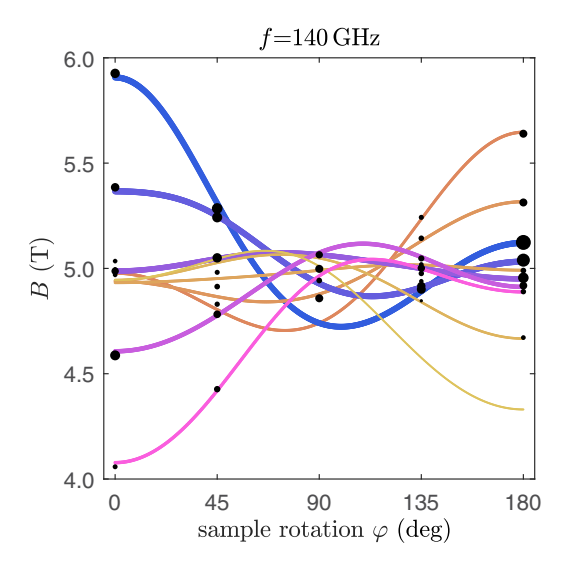


FIG. 5. Resonance field road map for Fe³⁺ at 140 GHz depicting model-calculated values (color) and such independently extracted from the experimental data (block symbols). Symbol sizes and line thickness represent the relative resonance amplitudes. For the calculated data, purple colors refer to Fe on octahedral Ga_{ii} sites while orange colors represent Fe on tetrahedral Ga_{i} sites. Note that some data points are shifted here due to a slight sample tilt and azimuthal off-angle which are considered in the evaluation but cannot be applied to the experimental data points in the graphical representation here. This is particularly the case at 0° , 45° and 90° sample orientation. These slight sample tilts removed the apparent discrepancies.

report the parameters for the spin Hamiltonian in Tables I and II for $\tilde{F}e^{3+}$ on octahedral \tilde{Ga}_{ii} and tetrahedral Ga_i sites, respectively. For Fe³⁺ on Ga_i, the complete ZFS parameters (Table II) are determined for the first time, to the best of our knowledge. Notably, both second and fourth-order ZFS parameters are smaller in absolute value than for Fe³⁺ on Gaii. Only for Gaii, another report of such a full parameter set could be found in the literature. It was obtained with X-band EPR by Meil'man [41]. Comparison of the parameter values is not directly possible because of different conventions for the orientation and rotation in the monoclinic plane relative to the crystallographic axes. However, by applying the parameters obtained in this work to Meil'man's data, some conclusions can be drawn. (See supplement for an overlay of data from Ref. [41] with modeled data based on the parameters reported here.) While the angle between $x_{\text{Meil'man}}$ (the coordinate system in which the ZFS coefficients are presented) and a, $\angle(x_{\text{Meil'man}}, a)$, is mentioned to be 115° for Meil'man's report, we find that it is rather approximately 99° based on our Hamiltonian parameters; or equivalently $\angle(x_{\text{Meil'man}}, c^*) \approx 9^{\circ} \mod 180^{\circ}$. Considering such a 9° angle offset between $x'_{\rm Meil'man}$ (the principal orientation of the g-factor tensor) and c^* , ZFS parameters for the octahedral Gaii sites were computed from Ref. [41] in the same convention as used throughout this paper. The obtained values are shown in the last column of Table I. It appears that the signs of all parameters are inverted. This is a result of the limitations of single-frequency X-band EPR for a system with large ZFS compared with the multiple frequency approach at high field as employed here. From our experimental data

TABLE I. Parameters for full Hamiltonian for Fe³⁺ on octahedral Ga_{ii} site. The convention $(x, y, z) \parallel (c^*, a, b)$ is assumed. Reported error limits are estimated from comparing the range of different solutions found by global optimization. Second- and fourth-order values computed by crystal-ligand-field theory are given as relative numbers normalized to B_2^0 and B_4^0 , respectively, with the original signs. The absolute values obtained are $B_2^0 = -10\,100$ GHz and $B_4^0 = -2800$ GHz.

	This work Expt.	This work CLFT	Meil'man Ref. [41]
B_2^2 (MHz)	-1932 ± 1	1.24	1908 a
$B_2^{\tilde{0}}$ (MHz)	-2312 ± 2	-1	2212
B_2^{-2} (MHz)	-830 ± 6	-1.34	891 <mark>a</mark>
$B_4^{\overline{4}}$ (MHz)	17.3 ± 0.1	13.6	-13.4^{a}
B_4^2 (MHz)	19.0 ± 0.5	33.8	-16.2^{a}
B_4^0 (MHz)	-0.4 ± 0.1	-1	1.0
B_4^{-2} (MHz)	-13.7 ± 0.2	-17.3	11.0 ^a
B_4^{-4} (MHz)	-14.3 ± 0.3	-21.9	19.5ª
$g_{x'}$	2.006 ± 0.001		2.004
$g_{y'}$	2.000 ± 0.001		2.002
$g_z = g_b$	2.001 ± 0.001		2.007
$\angle(x', c^*)$ for \hat{g} (°)	46.1 ± 1		$\approx 9 \text{ (or } 39)^{\text{b}}$

^a Values computed from reported values and applied rotation of -9° around z.

with all five transitions appearing in each B scan, the sign of particularly B_2^0 is unambiguously given by the relative transition amplitudes which result from state occupation following a Boltzmann distribution. The different sign for Meil'man's parameters was already noted by Büscher and Lehmann [39]. Apart from this, the overall shape of the ZFS Hamiltonian matches very well. Only the g-factor anisotropy differs sig-

TABLE II. Parameters for full Hamiltonian for Fe³⁺ on tetrahedral Ga_i site. The convention $(x,y,z) \parallel (c^*,a,b)$ is assumed. Reported error limits are estimated from comparing the range of different solutions found by global optimization. Second- and fourth-order values computed by crystal-ligand-field theory are given as relative numbers normalized to B_2^0 and B_4^0 , respectively, with original signs. The absolute values obtained are $B_2^0 = -2900$ GHz and $B_4^0 = -3100$ GHz.

	Expt.	CLFT
$\overline{B_2^2 \text{ (MHz)}}$	1328 ± 2	-4.83
$B_2^{\tilde{0}}$ (MHz)	-1666 ± 2	-1
B_2^{-2} (MHz)	-1238 ± 3	1.55
B_4^{4} (MHz)	11.7 ± 0.2	-2.26
B_4^2 (MHz)	2.1 ± 0.3	-17.0
B_4^0 (MHz)	-2.4 ± 0.1	1
B_4^{-2} (MHz)	-4.0 ± 0.5	10.0
B_4^{-4} (MHz)	-2.3 ± 3.2	7.23
$g_{x'}$	1.900 ± 0.010	
$g_{v'}$	2.115 ± 0.010	
$g_z = g_b$	2.131 ± 0.010	
$\angle(x', c^*)$ for \hat{g} (°)	47.6 ± 1	

^bValue estimated from parameters obtained in this work applied to Meil'man's data, see text.

nificantly between Meil'man and the values reported here. This originates most likely from a generally lower sensitivity to \hat{g} compared with the ZFS coefficients at the high frequencies at which we observe the EPR resonances (Table I). The ZFS here has a much stronger effect than the small g-factor anisotropy that modifies the spin resonances only by approximately $\Delta g \mu_{\rm B} B \approx 0.5$ GHz at most. Overall, a better accuracy is expected from the multifrequency approach used here. Regarding the principal directions of the g-factor tensor (x', y'), we note that the angle scale in the plot of Meil'man's report is offset by 15°, i.e., the $x'_{\text{Meil'man}}$ axis points at nominal 15° of their laboratory coordinate system. Hypothetically assuming the $x'_{\text{Meil'man}}$ axis would actually point at -15° therein would render $\angle(x'_{\text{Meil'man}}, c^*)$ from $\approx 9^\circ$ rather to 39° and hence seem more plausible when compared with the here-reported angle of approximately 46°.

Qualitative estimates for the structure of the ZFS of the monoclinic Fe3+ on octahedral Gaii site are obtained from CLFT. Computed values in the same reference coordinate system as above are presented the middle column of Table I. The absolute values differ by several orders of magnitude as the single-charge model appears to greatly overestimate the ligand-induced perturbation. However, in terms of relative size (e.g., comparing B_4^0 vs B_4^2 vs B_4^4), the computed parameter values represent a structure, i.e., relative order of parameters, for the fourth-order terms that is very close to the experimental results shown in Table I: Except for B_2^2 , all signs match the experimentally found ones. All value ratios are very similar to the experimental results, even with B_4^0 having clearly the smallest magnitude. This does not only confirm the experimental findings but also allows us to conclude that the nearest-neighbor oxygen atoms are the main origin for monoclinic-symmetry imprints on the local electronic structure of Fe³⁺. However, the qualitative match of the second-order terms appears significantly less accurate. This could imply that higher-order perturbations, e.g., orbital effects and spin dipole interactions, make a significantly larger contribution to the second-order terms.

Computed Hamiltonian parameter values for Fe³⁺ on Ga_i sites are shown in the last column of Table II. These values do not provide as reasonable agreement as found for the Gaii sites. A reason for the observed disagreement may be found in the actual choice for the Fe-O bond-length parameters. The calculated Hamiltonian parameters depend strongly on the computed unit-cell dimensions. Therefore, the PBE-sol functional was used, which generally tends to agree very well in structure for semiconductors. Small variations in the structural parameters do not change the sign of the Hamiltonian values or significantly affect the relative magnitudes of the computed ZFS components. The values do also not change order with respect to their signature and magnitude within their parameter set when more neighbors are included into the CLFT computations. Yet, the B_{\perp}^{q} coefficients are most sensitive to the details of the structure (see the Supplemental Material [47]). This latter observation is reasonable because the fourth-order B_{4}^{q} coefficients should be most sensitive to the local symmetry elements of the defect. The Gaii site features near-octahedral local symmetry, the related electrostatic Hamiltonian is likely more constraining and more well-described by the qualities of the CLFT model than the Gai site, which features a lower,

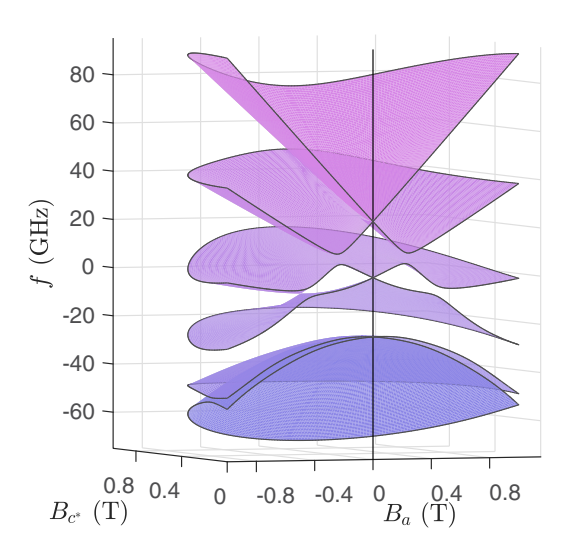


FIG. 6. Splitting of the six states of Fe on Ga_{ii} for B up to 1 T applied inside the monoclinic plane (B_a being the contribution of \vec{B} parallel to a, B_{c^*} the one parallel to c^*). The crystallographic a axis is rather close to a main principal direction of the ZFS defined by the rotation around b which is required to reach $B_2^{-2} = 0$. Nevertheless, the effect of the lowered monoclinic symmetry is clearly visible. At zero B, the splittings between $|m_s| = 1/2$, $|m_s| = 3/2$, and $|m_s| = 5/2$ are approx. 24 GHz each. For higher fields, the state anticrossings result in a swap of the states' spin quantum number.

near-tetrahedral local symmetry. At present, it remains difficult to determine the exact degree of complexity required for this method to yield sufficiently accurate ZFS components, specifically for the Fe^{3+} defects in the Ga_i and Ga_{ii} sites, but also for general defects within low-symmetry environments. Our finding here underlines the need for improved theoretical methods for modeling the effective spin Hamiltonian in low-symmetry materials.

All coefficients of the ZFS Hamiltonian are reported here with respect to a coordinate system that is pinned to the crystallographic axes such that $(x, y, z) \equiv (c^*, a, b)$. To understand the orientation of the main components, we can find the angle that is required to rotate the coordinate system around z||b such that $B_2^{-2} = 0$. For Fe³⁺ on Ga_{ii} sites, this is approximately 11.6°. For Ga_i sites, it is significantly different with approximately -21.5° . Figure 6 illustrates the complex structure of the state energies for Fe³⁺ on the Ga_{ii} site when \vec{B} is applied within the monoclinic ac plane. For zero B field, the states with $|m_s| = 1/2, 3/2, 5/2$ are each twofold degenerate. All degeneracies are lifted at finite B and spin mixing yields state anticrossing. This means that m_s is no longer a well-defined quantum number at respective field direction and strength. Consequently, so-called forbidden transitions would become relevant. Due to the large ZFS, forbidden transitions may dominate at low frequencies like X-band. At high frequencies and higher fields, however, m_s is well-defined again, and the situation simplifies with clearly ordered, strong, allowed transitions dominating.

A. Comparison to the simplified spin Hamiltonian

The values of nearly all Stevens coefficients which are listed in Tables I and II appear non-negligible. Particularly

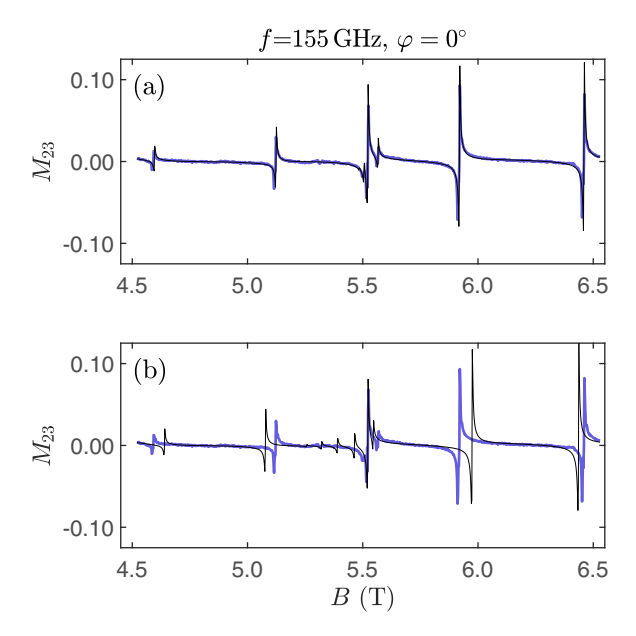


FIG. 7. Comparison of experimental and best-matching model data for Müller matrix element M_{23} at 155 GHz for sample orientation 0° . (a) Modeling based on the full fourth-order monoclinic Hamiltonian (1). (b) Based on the simplified second-order orthorhombic model that is often used. Note that the five strong lines from Fe on Ga_{ii} site are equidistant for the simplified model but not in the experimental data.

fourth-order parameters, including those with negative indices, must not be ignored. Regarding the generally much smaller values of fourth-order parameters, it should be noted that the reported values B_k^q here are unscaled ones. Upon scaling (i.e., conversion to $b_k^{\hat{q}}$), fourth-order coefficients would be 20 times enhanced compared with second-order ones ($b_2^q =$ $3B_2^q$, $b_4^q = 60B_4^q$, see Supplemental Material [47]). This emphasizes the significance of the fourth-order contributions. For further discussion and for comparison to earlier reports on EPR of Fe in monoclinic β -Ga₂O₃, we modeled our data also with the simplified Hamiltonian of Eq. (2). The application of the simplified Hamiltonian results in a large mismatch for some particular measurement configurations, as shown in Fig. 7. In this case, the Hamiltonian (2) can principally not describe the nonequidistant resonances that are observed in the B scan. Nevertheless, model parameters D and E for the best-matching model are presented in Tables III and IV. To compare these values to calculations from first principles, DFT was applied to Fe^{3+} on Ga_{ii} sites, and Table III shows the computed parameter values. Compared with our experimental results, they are off by factors of three and five for D and E, respectively. However, we notice that the sign of D is found correctly. Also the order of magnitude is consistent. Possible issues preventing better match with the experimental data may arise from uncertainties in the functional description of d orbitals even when using HSE, e.g., arising from a lack of accurate screening and over-localization [75,76], or spin-orbit effects [60].

When comparing the different reported D and E values in Tables III and IV, main discrepancies are seen for their signs. While the sign of E can be swapped by rotating the coordinate system 90° around z, the sign of D is unique and clearly determined from our experimental data through the relative transition amplitudes of the five transitions in a quintuplet. Büscher and Lehmann reported the same signs as we found for Fe³⁺ on the Ga_{ii} site (and thereby corrected Meil'man, see above) by combining X-band and O-band EPR, and their temperature dependencies. However, probably due to lower sensitivity for the lower density of Fe³⁺ on the Ga_i site, the signs in Büscher and Lehmann's report are opposite for this tetrahedral coordination. Other studies did not focus on the sign through comparison of relative transition amplitudes. Regarding the absolute D and E parameters, it appears that all single-frequency studies found slightly smaller values than the multifrequency approach presented here. This finding seems independent of the probe frequency used. Even the 94 GHz study by Babunts et al. derived smaller values. This could be an effect of correlation between \hat{g} and the ZFS parameters. Modeling ZFS coefficients simultaneously with the g factor suffers from large parameter correlation. This can be widely overcome through involving multiple frequencies. Only Büscher and Lehmann involved at least two frequencies. However, as they needed to obtain EPR data at different setups, implying different alignment off-angles for the different frequencies, they could not fit the \hat{g} factor either, Instead, they assumed a constant value. In experiments with low-symmetry crystals, alignment off-angles are unavoidable. It is therefore of utmost importance to be able to measure a sample at multiple frequencies without need for realignment or, e.g., switching the experimental setup. Only few experimental setups are capable of this [77,78].

TABLE III. Parameters of the simplified second-order Hamiltonian for Fe^{3+} on octahedral Ga_{ii} site. Büscher and Lehmann, and Bhandari and Zvanut assumed fixed isotropic g factors (respective values are here printed in angled brackets and are not results). The orientation of the principal direction was not reported by Bhandari and Zvanut, and by Babunts $et\ al$. The reported coordinates system of Büscher and Lehmann is left handed.

	This work Expt.	This work DFT	Büscher Ref. [39]	Bhandari Ref. [36]	Babunts Ref. [37]
$D = 3B_2^0 \text{ (MHz)}$	-6930	-2222	-6300	6624	6320
$E = B_2^2 \text{ (MHz)}$	-2100	-410	-2060	2049	-2550
$\angle(x,c*)$ (°)	11.6	13.77	12.3		
(g_x,g_y)	(2.000, 2.006)		[(2.0023, 2.0023)]	[(2.0043, 2.0043)]	(2.004, 2.002)
$g_z = g_b$	2.001		[2.0023]	[2.0043]	2.007

TABLE IV. Parameters for simplified Hamiltonians for Fe^{3+} on tetrahedral Ga_i site. Büscher and Lehmann, and Bhandari and Zvanut assumed fixed isotropic g factors (respective values are printed here in angled brackets and are not results). The orientation of the principal direction was not reported by Bhandari and Zvanut, and by Babunts $et\ al.$

	This work Expt.	Büscher Ref. [39]	Bhandari Ref. [36]	Babunts Ref. [37]
$D = 3B_2^0 \text{ (MHz)}$	-4980	4725	4707	4221
$E = B_2^2 \text{ (MHz)}$	-1820	1349	1335	-1740
$\angle(x, c*)$ (°)	70	95		
(g_x,g_y)	(2.1, 1.9)	[(2.0023, 2.0023)]	[(2.0043, 2.0043)]	(2.004, 2.002)
$g_z = g_b$	2.1	[2.0023]	[2.0043]	2.007

In conclusion, fourth-order, monoclinic-symmetry terms are of high importance and it is necessary to measure at different and particularly at high frequency to obtain them reliably [79]. The orthorhombic second-order Hamiltonian represents an insufficient approximation for Fe_{Ga} in monoclinic β -Ga₂O₃. Modeling was also tested based on a fourth-order orthorhombic spin Hamiltonian but did not prove successful either.

B. Outlook

Particular interest in investigating Fe-doped β -Ga₂O₃ with high field/high frequency (HF) EPR originates from the fact that integer spin systems like Fe²⁺ may become accessible at large EPR probe frequencies and/or fields. The possible EPR observation of Fe²⁺ has recently been reported using a 94 GHz system [37]. Yet, only one transition was observed, and even higher frequencies are required to verify the report and improve the accuracy of the parameters of the spin Hamiltonian. The problem of detecting integer spin systems with conventional EPR systems arises generally as soon as ZFS exceeds the microwave frequency used (e.g., X band around 10 GHz). In such cases, transitions with $\Delta m_s = \pm 1$ would only become accessible at very high magnetic fields [80]. Therefore, only few integer-spin (e.g., triplet) systems are accessible by conventional EPR systems. For integer-spin systems with large ZFS, conventional EPR frequencies would mostly give access to transitions referred to as $\Delta m_s = \pm 2, 4, \dots$ Due to state hybridization and the spin quantum number being not a well-defined quantity, these transitions do actually not transfer angular momentum in the indicated way. Hence, $\Delta m_s = 0$ would be a more appropriate notation [80]. Detection of such nominally forbidden transitions typically requires parallel-mode EPR systems where the polarization of the microwave's magnetic field $\vec{\mathcal{B}}_1$ coincides with the external field \vec{B} . An ellipsometric approach could provide further insights here by analyzing the exact transition polarization. Still, if transition frequencies vary only slightly with the external magnetic field, B-domain EPR can reveal very large broadening that often prohibits detection [81]. A way out of these issues can be HF-EPR with the EPR probe frequency larger than the ZFS which allows direct access to $\Delta m_s = \pm 1$ transitions. Flexible choice of the frequency can enable new observations here.

VI. CONCLUSION

The ability to perform EPR measurements at high field and frequency and to vary the frequency without sample realignment is of utmost importance for the study of anisotropic high-spin systems. Only this possibility allows truly disentangling the anisotropic ĝ-factor and ZFS contributions. To do so, we have applied THz ellipsometry at frequencies between 110 and 170 GHz and fields between 3 and 7 T to study Fe^{3+} in monoclinic β -Ga₂O₃. This unique method enables frequency-varying, cavity-free EPR experiments. We report complete parameters for fourth-order monoclinic spin Hamiltonians, including for Fe³⁺ on tetrahedral Ga_i sites. We compared our results to earlier reports and verify unambiguously the sign of the ZFS parameters. Furthermore, our experimental results demonstrate clearly that approximate second-order orthorhombic spin models are insufficient for these systems. We have compared our findings with theoretical computations and find a match of the order of the expected second-order ZFS parameters with DFT calculations, and a partial qualitative match of the fourth-order structure with ligand-field theory. Here, there is a need for further improved theoretical methods. We expect that the new experimental approach demonstrated will in a future study allow obtaining precise spin-Hamiltonian parameters for Fe²⁺ which is the most relevant charge state acting as a compensating acceptor.

ACKNOWLEDGMENTS

This work was performed in the framework of the grant "Wide-band gap semiconductors for next generation quantum components" supported by the Knut and Alice Wallenberg Foundation (Grant No. 2018.0071), and with funding from the Swedish Research Council VR under Grants No. 2016-00889 and No. 2022-04812. We acknowledge further support from the National Science Foundation (NSF) under Award No. NSF/EPSCoR RII Track-1: Emergent Quantum Materials and Technologies (EQUATE), Award No. OIA-2044049, by the Air Force Office of Scientific Research under Awards No. FA9550-19-S-0003, No. FA9550-21-1-0259, and No. FA9550-23-1-0574 DEF, the Swedish Energy Agency under Award No. P45396-1, the Swedish Governmental Agency for Innovation Systems (VINNOVA) under the Competence Center Program Grant No. 2022-03139, the Swedish Foundation for Strategic Research under Grants No.

RIF14-055 and No. EM16-0024, and the Swedish Government Strategic Research Area NanoLund and in Materials Science on Functional Materials at Linköping University, Faculty Grant SFO Mat LiU No. 2009-00971. M.S. acknowledges the University of Nebraska Foundation and the J. A. Woollam Foundation for financial support. Parts of the computations were enabled by resources provided by the National Academic Infrastructure for Supercomputing in Sweden (NAISS) and the Swedish National Infrastructure for Computing (SNIC) at NSC, partially funded by the Swedish Research Council through Grant Agreements No. 2022-06725 and No. 2018-05973. V.I. acknowledges support from the National Research, Development, and Innovation Office of Hungary within the Quantum Information National Laboratory of Hungary (Grant No. 2022-2.1.1-NL-2022-00004) and within Grant No. FK 145395. S.M. was supported by the U.S. Department of Energy, Office of Science, National Quantum Information Science Research Centers, Co-design Center for Quantum Advantage (C2QA) under Contract No. DE-SC0012704. C.G.V.d.W. was supported by the GAME MURI of the Air Force Office of Scientific Research (FA9550-18- 1-0479). Use was made of computational facilities purchased with funds from the National Science Foundation (CNS-1725797) and administered by the Center for Scientific Computing (CSC). The CSC is supported by the California NanoSystems Institute and the Materials Research Science and Engineering Center (MRSEC; NSF DMR 2308708) at UC Santa Barbara. This work also used Expanse at SDSC through allocation DMR070069 from the Extreme Science and Engineering Discovery Environment (XSEDE), which was supported by National Science Foundation Grant No. #1548562.

- [1] M. Higashiwaki, β-gallium oxide devices: Progress and outlook, Phys. Status Solidi RRL **15**, 2100357 (2021).
- [2] Gallium Oxide, Springer Series in Materials Science, edited by M. Higashiwaki and S. Fujita (Springer, Cham, 2020), Vol. 293.
- [3] S. J. Pearton, F. Ren, M. Tadjer, and J. Kim, Perspective: Ga₂O₃ for ultra-high power rectifiers and MOSFETS, J. Appl. Phys. 124, 220901 (2018).
- [4] S. J. Pearton, J. Yang, P. H. Cary, F. Ren, J. Kim, M. J. Tadjer, and M. A. Mastro, A review of Ga₂O₃ materials, processing, and devices, Appl. Phys. Rev. 5, 011301 (2018).
- [5] J. Shi, J. Zhang, L. Yang, M. Qu, D.-C. Qi, and K. H. L. Zhang, Wide bandgap oxide semiconductors: From materials physics to optoelectronic devices, Adv. Mater. 33, 2006230 (2021).
- [6] Z. Galazka, β -Ga₂O₃ for wide-bandgap electronics and optoelectronics, Semicond. Sci. Technol. **33**, 113001 (2018).
- [7] K. D. Chabak, K. D. Leedy, A. J. Green, S. Mou, A. T. Neal, T. Asel, E. R. Heller, N. S. Hendricks, K. Liddy, A. Crespo, N. C. Miller, M. T. Lindquist, N. A. Moser, R. C. Fitch, D. E. Walker, D. L. Dorsey, and G. H. Jessen, Lateral β-Ga₂O₃ field effect transistors, Semicond. Sci. Technol. 35, 013002 (2020).
- [8] A. J. Green, J. Speck, G. Xing, P. Moens, F. Allerstam, K. Gumaelius, T. Neyer, A. Arias-Purdue, V. Mehrotra, A. Kuramata, K. Sasaki, S. Watanabe, K. Koshi, J. Blevins, O. Bierwagen, S. Krishnamoorthy, K. Leedy, A. R. Arehart, A. T. Neal, S. Mou *et al.*, β-gallium oxide power electronics, APL Mater. 10, 029201 (2022).
- [9] K. Irmscher, Z. Galazka, M. Pietsch, R. Uecker, and R. Fornari, Electrical properties of β-Ga₂O₃ single crystals grown by the Czochralski method, J. Appl. Phys. 110, 063720 (2011).
- [10] T. Onuma, S. Fujioka, T. Yamaguchi, M. Higashiwaki, K. Sasaki, T. Masui, and T. Honda, Correlation between blue luminescence intensity and resistivity in β-Ga₂O₃ single crystals, Appl. Phys. Lett. 103, 041910 (2013).
- [11] Z. Galazka, K. Irmscher, R. Uecker, R. Bertram, M. Pietsch, A. Kwasniewski, M. Naumann, T. Schulz, R. Schewski, D. Klimm, and M. Bickermann, On the bulk β-Ga₂O₃ single crystals grown by the Czochralski method, J. Cryst. Growth 404, 184 (2014).
- [12] A. Y. Polyakov, N. B. Smirnov, I. V. Shchemerov, S. J. Pearton, F. Ren, A. V. Chernykh, and A. I. Kochkova, Electrical prop-

- erties of bulk semi-insulating β -Ga₂O₃ (Fe), Appl. Phys. Lett. **113**, 142102 (2018).
- [13] M. E. Ingebrigtsen, J. B. Varley, A. Y. Kuznetsov, B. G. Svensson, G. Alfieri, A. Mihaila, U. Badstübner, and L. Vines, Iron and intrinsic deep level states in Ga₂O₃, Appl. Phys. Lett. 112, 042104 (2018).
- [14] S. Bhandari and M. E. Zvanut, Charge trapping at Fe due to midgap levels in Ga₂O₃, J. Appl. Phys. 129, 085703 (2021).
- [15] A. Y. Polyakov, N. B. Smirnov, I. V. Schemerov, A. V. Chernykh, E. B. Yakimov, A. I. Kochkova, A. N. Tereshchenko, and S. J. Pearton, Electrical properties, deep levels and luminescence related to Fe in bulk semi-insulating β-Ga₂O₃ doped with Fe, ECS J. Solid State Sci. Technol. 8, Q3091 (2019).
- [16] N. Zhang, H. Liu, Q. Sai, C. Shao, C. Xia, L. Wan, Z. C. Feng, and H. F. Mohamed, Structural and electronic characteristics of Fe-doped β-Ga₂O₃ single crystals and the annealing effects, J. Mater. Sci. 56, 13178 (2021).
- [17] M. Schubert, R. Korlacki, S. Knight, T. Hofmann, S. Schöche, V. Darakchieva, E. Janzén, B. Monemar, D. Gogova, Q.-T. Thieu, R. Togashi, H. Murakami, Y. Kumagai, K. Goto, A. Kuramata, S. Yamakoshi, and M. Higashiwaki, Anisotropy, phonon modes, and free charge carrier parameters in monoclinic β-gallium oxide single crystals, Phys. Rev. B 93, 125209 (2016).
- [18] C. Sturm, R. Schmidt-Grund, C. Kranert, J. Furthmüller, F. Bechstedt, and M. Grundmann, Dipole analysis of the dielectric function of color dispersive materials: Application to monoclinic Ga₂O₃, Phys. Rev. B 94, 035148 (2016).
- [19] M. Schubert, A. Mock, R. Korlacki, S. Knight, Z. Galazka, G. Wagner, V. Wheeler, M. Tadjer, K. Goto, and V. Darakchieva, Longitudinal phonon plasmon mode coupling in β-Ga₂O₃, Appl. Phys. Lett. 114, 102102 (2019).
- [20] V. C. Agulto, K. Toya, T. N. K. Phan, V. K. Mag-usara, J. Li, M. J. F. Empizo, T. Iwamoto, K. Goto, H. Murakami, Y. Kumagai, N. Sarukura, M. Yoshimura, and M. Nakajima, Anisotropic complex refractive index of β-Ga₂O₃ bulk and epilayer evaluated by terahertz time-domain spectroscopy, Appl. Phys. Lett. 118, 042101 (2021).
- [21] N. Blumenschein, C. Kadlec, O. Romanyuk, T. Paskova, J. F. Muth, and F. Kadlec, Dielectric and conducting properties of

- unintentionally and Sn-doped β -Ga₂O₃ studied by terahertz spectroscopy, J. Appl. Phys. **127**, 165702 (2020).
- [22] P. Gopalan, S. Knight, A. Chanana, M. Stokey, P. Ranga, M. A. Scarpulla, S. Krishnamoorthy, V. Darakchieva, Z. Galazka, K. Irmscher, A. Fiedler, S. Blair, M. Schubert, and B. Sensale-Rodriguez, The anisotropic quasi-static permittivity of single-crystal β-Ga₂O₃ measured by terahertz spectroscopy, Appl. Phys. Lett. 117, 252103 (2020).
- [23] C. Sturm, J. Furthmüller, F. Bechstedt, R. Schmidt-Grund, and M. Grundmann, Dielectric tensor of monoclinic Ga₂O₃ single crystals in the spectral range 0.5–8.5 eV, APL Mater. 3, 106106 (2015).
- [24] C. Sturm and M. Grundmann, Singular optical axes in biaxial crystals and analysis of their spectral dispersion effects in β -Ga₂O₃, Phys. Rev. A **93**, 053839 (2016).
- [25] A. Mock, R. Korlacki, C. Briley, V. Darakchieva, B. Monemar, Y. Kumagai, K. Goto, M. Higashiwaki, and M. Schubert, Band-to-band transitions, selection rules, effective mass, and excitonic contributions in monoclinic β -Ga₂O₃, Phys. Rev. B **96**, 245205 (2017).
- [26] M. Yamaga, H. Tsuzuki, S. Takano, E. G. Villora, and K. Shimamura, Electron-spin resonance of transparent conductive oxide β -Ga₂O₃, J. Non-Cryst. Solids **358**, 2458 (2012).
- [27] N. T. Son, K. Goto, K. Nomura, Q. T. Thieu, R. Togashi, H. Murakami, Y. Kumagai, A. Kuramata, M. Higashiwaki, A. Koukitu, S. Yamakoshi, B. Monemar, and E. Janzén, Electronic properties of the residual donor in unintentionally doped β-Ga₂O₃, J. Appl. Phys. 120, 235703 (2016).
- [28] B. E. Kananen, L. E. Halliburton, E. M. Scherrer, K. T. Stevens, G. K. Foundos, K. B. Chang, and N. C. Giles, Electron paramagnetic resonance study of neutral Mg acceptors in β -Ga₂O₃ crystals, Appl. Phys. Lett. **111**, 072102 (2017).
- [29] N. C. Giles and L. E. Halliburton, 8-electron paramagnetic resonance (EPR) from β-Ga₂O₃ crystals, in *Gallium Oxide*, Metal Oxides, edited by S. Pearton, F. Ren, and M. Mastro (Elsevier, 2019), pp. 169–190.
- [30] J. E. Stehr, D. M. Hofmann, J. Schörmann, M. Becker, W. M. Chen, and I. A. Buyanova, Electron paramagnetic resonance signatures of Co^{2+} and Cu^{2+} in $\beta\text{-Ga}_2\text{O}_3$, Appl. Phys. Lett. 115, 242101 (2019).
- [31] C. A. Lenyk, N. C. Giles, E. M. Scherrer, B. E. Kananen, L. E. Halliburton, K. T. Stevens, G. K. Foundos, J. D. Blevins, D. L. Dorsey, and S. Mou, Ir⁴⁺ ions in β-Ga₂O₃ crystals: An unintentional deep donor, J. Appl. Phys. **125**, 045703 (2019).
- [32] S. Bhandari, M. E. Zvanut, and J. B. Varley, Optical absorption of Fe in doped Ga₂O₃, J. Appl. Phys. **126**, 165703 (2019).
- [33] C. A. Lenyk, T. D. Gustafson, L. E. Halliburton, and N. C. Giles, Deep donors and acceptors in β -Ga₂O₃ crystals: Determination of the Fe^{2+/3+} level by a noncontact method, J. Appl. Phys. **126**, 245701 (2019).
- [34] H. J. von Bardeleben, S. Zhou, U. Gerstmann, D. Skachkov, W. R. L. Lambrecht, Q. D. Ho, and P. Deák, Proton irradiation induced defects in β-Ga₂O₃: A combined EPR and theory study, APL Mater. 7, 022521 (2019).
- [35] C. A. Lenyk, T. D. Gustafson, S. A. Basun, L. E. Halliburton, and N. C. Giles, Experimental determination of the (0/-) level for Mg acceptors in β -Ga₂O₃ crystals, Appl. Phys. Lett. **116**, 142101 (2020).

- [36] S. Bhandari and M. E. Zvanut, Optical transitions for impurities in Ga₂O₃ as determined by photo-induced electron paramagnetic resonance spectroscopy, J. Appl. Phys. 127, 065704 (2020).
- [37] R. A. Babunts, A. S. Gurin, E. V. Edinach, H.-J. Drouhin, V. I. Safarov, and P. G. Baranov, Non-Kramers iron S = 2 ions in β -Ga₂O₃ crystals: High-frequency low-temperature EPR study, J. Appl. Phys. **132**, 155703 (2022).
- [38] N. T. Son, Q. D. Ho, K. Goto, H. Abe, T. Ohshima, B. Monemar, Y. Kumagai, T. Frauenheim, and P. Deák, Electron paramagnetic resonance and theoretical study of gallium vacancy in β-Ga₂O₃, Appl. Phys. Lett. 117, 032101 (2020).
- [39] R. Büscher and G. Lehmann, Correlation of zero-field splittings and site distortions. IX. Fe³⁺ and Cr³⁺ in β-Ga₂O₃, Z. Naturforsch., A: Phys. Sci. 42, 67 (1987).
- [40] D. Toloman, A. Popa, M. Stan, T. D. Silipas, and A. R. Biris, Identification of different iron sites in β -Ga₂O₃ nanoparticles by spectroscopic methods, AIP Conf. Proc. **1700**, 060005 (2015).
- [41] M. L. Meil'man, EPR of Fe³⁺ ions in β -Ga₂O₃ crystals, Sov. Phys. Solid State **11**, 1403 (1969).
- [42] W. Gunsser and K. Rohwer, Determination of the correlation between the crystal field axis system and the crystallographic axes in chromium-doped β -Ga₂O₃ by EPR, Phys. Status Solidi B **116**, 275 (1983).
- [43] T. Yeom, I. G. Kim, S. H. Lee, S. H. Choh, and Y. M. Yu, Electron paramagnetic resonance characterization of Cr^{3+} impurities in a β -Ga₂O₃ single crystal, J. Appl. Phys. **93**, 3315 (2003).
- [44] T. D. Gustafson, C. A. Lenyk, L. E. Halliburton, and N. C. Giles, Deep donor behavior of iron in β -Ga₂O₃ crystals: Establishing the Fe^{4+/3+} level, J. Appl. Phys. **128**, 145704 (2020).
- [45] C. Rudowicz, On standardization and algebraic symmetry of the ligand field Hamiltonian for rare earth ions at monoclinic symmetry sites, J. Chem. Phys. **84**, 5045 (1986).
- [46] R. Boča, Zero-field splitting in metal complexes, Coord. Chem. Rev. 248, 757 (2004).
- [47] See Supplemental Material at http://link.aps.org/supplemental/ 10.1103/PhysRevB.109.214106 for additional plots of measured and modelled data, further details on the theoretical approaches, an overview of the relevant spin operators, and additional illustrations of frequency- and field-domain EPR of Fe³⁺.
- [48] K. Momma and F. Izumi, *VESTA 3* for three-dimensional visualization of crystal, volumetric and morphology data, J. Appl. Crystallogr. 44, 1272 (2011).
- [49] C. Rudowicz and R. Bramley, On standardization of the spin Hamiltonian and the ligand field Hamiltonian for orthorhombic symmetry, J. Chem. Phys. 83, 5192 (1985).
- [50] A. Abragam and B. Bleaney, Electron Paramagnetic Resonance of Transition Ions (Clarendon Press, Oxford, 1970).
- [51] P. Kühne, N. Armakavicius, V. Stanishev, C. M. Herzinger, M. Schubert, and V. Darakchieva, Advanced terahertz frequency-domain ellipsometry instrumentation for *in situ* and *ex situ* applications, IEEE Trans. Terahertz Sci. Technol. 8, 257 (2018).
- [52] M. Schubert, S. Knight, S. Richter, P. Kuehne, V. Stanishev, A. Ruder, M. Stokey, R. Korlacki, K. Irmscher, P. Neugebauer, and V. Darakchieva, Terahertz electron paramagnetic resonance generalized spectroscopic ellipsometry: The magnetic response

- of the nitrogen defect in 4H-SiC, Appl. Phys. Lett. **120**, 102101 (2022).
- [53] H. Fujiwara, Spectroscopic Ellipsometry: Principles and Applications (John Wiley & Sons, Chichester, 2007).
- [54] R. A. Chipman, Polarimetry, in *Handbook of Optics*, edited by M. Bass (McGraw-Hill, New York, 1995), Chap. 22.
- [55] J. W. Orton, *Electron Paramagnetic Resonance: An Introduction to Transition Group Ions in Crystals* (Iliffe, London, 1968).
- [56] H. Aida, K. Nishiguchi, H. Takeda, N. Aota, K. Sunakawa, and Y. Yaguchi, Growth of β -Ga₂O₃ single crystals by the edge-defined, film fed growth method, Jpn. J. Appl. Phys. 47, 8506 (2008).
- [57] A. Kuramata, K. Koshi, S. Watanabe, Y. Yamaoka, T. Masui, and S. Yamakoshi, High-quality β-Ga₂O₃ single crystals grown by edge-defined film-fed growth, Jpn. J. Appl. Phys. 55, 1202A2 (2016).
- [58] S. Stoll and A. Schweiger, Easyspin, a comprehensive software package for spectral simulation and analysis in EPR, J. Magn. Reson. 178, 42 (2006).
- [59] J. Telser, EPR interactions—zero-field splittings, in *eMagRes* (John Wiley and Sons, Ltd., 2017), pp. 207–234.
- [60] S. Mu and K. D. Belashchenko, Influence of strain and chemical substitution on the magnetic anisotropy of antiferromagnetic Cr₂O₃: An *ab initio* study, Phys. Rev. Mater. 3, 034405 (2019).
- [61] A. Scheie, *PyCrystalField*: Software for calculation, analysis and fitting of crystal electric field Hamiltonians, J. Appl. Crystallogr. 54, 356 (2021).
- [62] M. T. Hutchings, Point-charge calculations of energy levels of magnetic ions in crystalline electric fields, Solid State Phys. 16, 227 (1964).
- [63] P. E. Blöchl, Projector augmented-wave method, Phys. Rev. B 50, 17953 (1994).
- [64] G. Kresse and J. Hafner, Ab initio molecular dynamics for open-shell transition metals, Phys. Rev. B 48, 13115 (1993).
- [65] G. Kresse and J. Furthmüller, Efficient iterative schemes for ab initio total-energy calculations using a plane-wave basis set, Phys. Rev. B 54, 11169 (1996).
- [66] J. Heyd, G. E. Scuseria, and M. Ernzerhof, Hybrid functionals based on a screened Coulomb potential, J. Chem. Phys. 118, 8207 (2003).
- [67] J. Heyd, G. E. Scuseria, and M. Ernzerhof, Erratum: "Hybrid functionals based on a screened Coulomb potential" [J. Chem. Phys. 118, 8207 (2003)], J. Chem. Phys. 124, 219906 (2006).
- [68] C. Freysoldt, J. Neugebauer, and C. G. Van de Walle, Fully ab initio finite-size corrections for charged-defect supercell calculations, Phys. Rev. Lett. 102, 016402 (2009).

- [69] C. Freysoldt, J. Neugebauer, and C. G. Van de Walle, Electrostatic interactions between charged defects in supercells, Phys. Status Solidi B 248, 1067 (2011).
- [70] M. J. Rayson and P. R. Briddon, First principles method for the calculation of zero-field splitting tensors in periodic systems, Phys. Rev. B 77, 035119 (2008).
- [71] V. Ivády, I. A. Abrikosov, and A. Gali, First principles calculation of spin-related quantities for point defect qubit research, npj Comput. Mater. 4, 76 (2018).
- [72] H. Xiang, C. Lee, H.-J. Kooc, X. Gonga, and M.-H. Whangbo, Magnetic properties and energy-mapping analysis, Dalton Trans. 42, 823 (2013).
- [73] J. Li, L. Gu, and R. Wu, Slow spin relaxation in single endohedral fullerene molecules, Phys. Rev. B 104, 224431 (2021).
- [74] J. P. Perdew, A. Ruzsinszky, G. I. Csonka, O. A. Vydrov, G. E. Scuseria, L. A. Constantin, X. Zhou, and K. Burke, Restoring the density-gradient expansion for exchange in solids and surfaces, Phys. Rev. Lett. 100, 136406 (2008).
- [75] V. Ivády, I. A. Abrikosov, E. Janzén, and A. Gali, Role of screening in the density functional applied to transitionmetal defects in semiconductors, Phys. Rev. B 87, 205201 (2013).
- [76] V. Ivády, R. Armiento, K. Szász, E. Janzén, A. Gali, and I. A. Abrikosov, Theoretical unification of hybrid-DFT and DFT + *U* methods for the treatment of localized orbitals, Phys. Rev. B 90, 035146 (2014).
- [77] P. Neugebauer, D. Bloos, R. Marx, P. Lutz, M. Kern, D. Aguilà, J. Vaverka, O. Laguta, C. Dietrich, R. Clérac, and J. van Slageren, Ultra-broadband EPR spectroscopy in field and frequency domains, Phys. Chem. Chem. Phys. 20, 15528 (2018).
- [78] G. Khatri, G. Fritjofson, J. Hanson-Flores, J. Kwon, and E. Del Barco, A 220 GHz-1.1 THz continuous frequency and polarization tunable quasi-optical electron paramagnetic resonance spectroscopic system, Rev. Sci. Instrum. 94, 034714 (2023).
- [79] H. Matsuoka, K. Furukawa, K. Sato, D. Shiomi, Y. Kojima, K. Hirotsu, N. Furuno, T. Kato, and T. Takui, Importance of fourth-order zero-field splitting terms in random-orientation EPR spectra of Eu(II)-doped strontium aluminate, J. Phys. Chem. A 107, 11539 (2003).
- [80] D. T. Petasis and M. P. Hendrich, A new Q-band EPR probe for quantitative studies of even electron metalloproteins, J. Magn. Reson. 136, 200 (1999).
- [81] M. P. Hendrich and P. G. Debrunner, Integer-spin electron paramagnetic resonance of iron proteins, Biophys. J. **56**, 489 (1989).